Seismicity and thermal structure of the St. Paul Transform System, equatorial Atlantic: Insights from focal depth analysis

Guilherme W. S. de Melo[1], Ingo Grevemeyer[1], Sibiao Liu[1], Marcia Maia[2], Lars Rüpke[1]

[1]GEOMAR Helmholtz Centre of Ocean Research Kiel, Kiel, Germany

[2]Geo-Ocean, University of Brest, CNRS, Ifremer, UMR6538, F-29280, Plouzane, France

Correspondence to: Guilherme de Melo (gdemelo@geomar.de)

Abstract

The slow-spreading Mid-Atlantic Ridge is segmented and offset by transform faults. Among these, the St. Paul Transform System (SPTS), located in the equatorial Mid-Atlantic Ridge, is a complex multi-fault system with four transform faults (Transform A, B, C, and D) and three intra-transform spreading segments with a cumulated offset of 630 km. The SPTS is seismically active, with strong strike-slip earthquakes reaching moment magnitudes of 6.9. In this study, we have re-analyzed the focal depth of 35 earthquakes of the Global Centroid Moment Tensor (GCMT) catalog with $5.3 \leq M_W \leq 6.9$ occurring at Transform A, B, and C since 2004, using regional surface waveform modelling. In addition, we derived a 3-dimensional half-space cooling thermal structure along the transform system that relates the focal depths to the temperature structure. Our results of focal depths indicated that the seismogenic zone of both Transform A, B, and C reaches from 5 to 18 km below the seafloor, with the deepest earthquakes located at the center area of the strike-slip segments, and shallower earthquakes occur towards the ridge-transform intersections. The comparison with the half-space cooling indicates that the deepest earthquakes are located in a cooler lithosphere located near the center of the transform segments, with their deformations reaching 600-900ºC. These observations challenge previous viscoplastic mantle geodynamic models that indicated a warm temperature toward the center of a transform fault. The main features found at the SPTS are supported by previous studies of focal depth in other transform faults in the Atlantic Ocean, supporting a global pattern and the occurrence of a cooler mantle at the center of the oceanic transform faults.

Short summary

The St. Paul Transform System on the equatorial Mid-Atlantic Ridge is a seismically active multi-fault system. This study re-examines the focal depths of 35 earthquakes (M_W 5.3-6.9) from Transforms A, B, and C. The data suggest that the seismogenic zone ranges from 5 to 18 km deep, with the deepest occurring in cooler lithosphere around the center of the transform segments. This challenges earlier hypotheses and indicates a global pattern of cooler mantle in center of oceanic transform faults.

1. Introduction

Transform faults in the equatorial Atlantic Ocean are among the largest and most complex in the world's oceans (e.g., *Bonatti 1990*). Among them, the St. Paul Transform System (SPTS) is a prominent multi-fault transform zone composed of four transform faults (Figure 1) separated by short ridge segments. The SPTS is seismically active, as evidenced by the high frequency of recorded events in seismological catalogs (*Francis et al. 1978; Wolfe et al. 1993; de Melo and Do Nascimento 2018; de Melo et al. 2021a; Parnell-Turner et al. 2022*) with moment magnitude reaching up 6.9 cataloged by the Global Centroid Moment Tensor (GCMT, *Ekstrom et al., 2012*), with strike-slip faulting focal mechanism occurring along the transform fault segments of the SPTS. In addition, some thrust faulting earthquakes were observed in the vicinity of the St. Peter and St. Paul islands in the northernmost transform fault (*Wolfe et al. 1993*). Unfortunately, GCMT solutions are subject to considerable epicentral uncertainties that can reach ~70 km in distance from the appropriate tectonic features (*Pan et al. 2002*), limiting their reliability in detailed tectonic analyses.

Characterizing the seismicity of oceanic transform faults is critical to understanding the physical properties of the oceanic lithosphere, such as earthquake depths and their distribution along the transform fault segments. Previous seismological studies of focal depth in oceanic transform faults found that the maximum depth of the brittle-ductile transition zone occurs at the center of the transform fault where the cooling is most pronounced, while shallower events are concentrated close to the ridge-transform intersections (*e.g. Bergman and Solomon 1988; Abercrombie and Ekström 2001*). However, it has been suggested that a viscous-plastic rheology approximates the behavior of the oceanic lithosphere best, resulting into warmer temperatures toward the middle of the transform (*Behn et 2007; Liu et al., 2023*). For the Blanco transform fault offsetting the intermediate spreading Juan de Fuca Ridge in the NW Pacific Ocean, Roland et al. (2010) showed the numerical simulation introducing a viscous-plastic rheology are able to yield the spatial distribution of earthquakes. Yet, earthquakes along the Blanco transform did not reveal a profound increase of focal depth near the center of the transform segments (*Ren et al. 2023*) as found for transform faults in the Atlantic Ocean (*Bergman and Solomon 1988*).

In this paper, we report the focal depth of 35 earthquakes of the SPTS cataloged by the GCMT with $M_W \geq 5.3$, using regional seismic stations at the equatorial Atlantic. We use regional waveform modelling of surface waves to relocate epicenters onto the appropriate surface trace of transform imaged in bathymetric data (*Maia et al. 2016*). In addition, the procedure yields focal depth, and we observe that deeper earthquakes are located mostly in the middle of the transform segments of the SPTS and centroids occur at temperatures of 600 to 900ºC. Therefore, our results of the focal depth solutions suggest that oceanic transform faults generally present deeper earthquakes toward their central and cooler domains.

2. Study area

2.1. Tectonics of the St. Paul Transform System

The St. Paul Transform System is a complex multi-transform system composed of four transforms named A, B, C, and D, that offset the axis of the Mid-Atlantic Ridge (MAR) by 303, 142, 88, and 53 km, respectively (*Schilling et al.* 1995; *Maia et al.* 2016). Within this system, three short intra-transform ridge (ITR) segments of the MAR axis have been identified (*Maia et al.* 2016). Transform A is slowly slipping at a rate of 27.71 mm/year (*DeMets et al 2010*). A prominent topographic feature along transform A is the Atobá Ridge, 200 km long and 30 km wide, that reaches the sea level at Saint Peter and Saint Paul Archipelago (SPSPA; 0˚55'N and 29˚38'W) (*Maia et al. 2016*). SPSPA is a set of 6 islets and 4 rocks composed of peridotite mylonite and alkaline ultramafic mantle rocks with different serpentinization degrees (*Melson et al.* 1967, *Hekinian et al.* 2000; *Campos et al. 2022*). Samples obtained from the submarine parts of the Atobá Ridge along the COLEMIA (COLd Mantle Exhumation and Intra-transform Accretion) cruise (*Maia et al.* 2016), either by dredging or by submersible, were also predominately serpentinized mantle rocks (*Hekinian et al.* 2000; *Maia et al.* 2016). *Maia et al.* (2016) constrained the age offset along the transform system (Figure S1) and revealed a low-density layer (LDL; Figure S2) beneath the SPTS, which is interpreted in terms of a layer of serpentinized mantle (limited at 500ºC) as the nature of the rock sampled at the seafloor suggests that the low density layer may represent serpentinized mantle rather than magmatic crust. Transform A is highly segmented and composed of a diversity of restraining bends and stepovers, which induce local transpression in the Atobá Ridge area resulting in the ridge uplift and consequent exhumation of the mantle rocks (*Maia et al.* 2016). The present-day uplift rate is estimated to be 1.5 mm/year (*Campos et al.* 2010). Bickert et al. (2023) showed that the fluid percolation in Transform A causes a grain size reduction and weakens the local fault strength along the eastern part of the Atobá Ridge. To the best of our knowledge, the Atobá Ridge is the largest known example of a push-up ridge in the oceanic lithosphere and the only case studied so far.

Transform B extends between the ~27.6˚ and 26.4˚W longitude range and is formed by a principal transform displacement zone (PTDZ) slowly slipping at 27.77 mm/year (*DeMets et al 2010*), with a deep valley reaching more than 5500 m beneath the sea level (bsl) close to the western ridge-transform

96   intersection (RTI) with ~4,000 m bsl in its middle part. Transform C is slipping at 27.83 mm/year (*DeMets*

97   *et al 2010*), extending between the ~26.3° and 25.55°W longitude range, with a deep valley reaching more

98   than 5000 m bsl. Transform D is the shortest transform, occurring between ~25.5° and 25.05° W, with a

99   transform valley reaching approximately 4500 m bsl. Long-lived oceanic core complexes exhuming mantle

100   rocks have been mapped along the segment between Transforms C and D, suggesting colder spreading

101   contexts (*Vincent et al 2023*).

102   2.2. Seismotectonics of the St. Paul Transform System

103   At Transform A, the local micro-seismicity has been recorded by a local station installed at SPSPA

104   islets (*de Melo and do Nascimento. 2018*), revealing a seismically active setting. Fault plane motions

105   analyzed by the GCMT along the SPTS (Figure 1b; Figure S3) indicate that most of the solutions are strike-

106   slip, consistent with the main transform fault orientations. However, at Transform A, some solutions differ

107   from the expected transform fault kinematics, confirming complex fault geometry and segmentation.

108   Previous studies reported compressive mechanisms, uncommon for transform fault areas, near the SPSPA

109   islets in Transform A (e.g. *Wolfe et al. 1993*). Wolfe et al (1993) identified focal depths reaching up to 14

110   km below seafloor (bsf) in earthquakes that occurred at Transform A, while Engeln et al. (1986) found in

111   strike-slip solutions with a focal depth of 3-7 km bsf at the same transform segment. Francis et al (1978)

112   reported microseismicity with focal depth reaching up to 11 km bsf at Transform D. Wolfe et al. (1993)

113   suggested that additional factors may control the occurrence of compressive earthquakes in Transform A,

114   such as recent changes in plate motion, differential lithospheric cooling, or the development of a weakened

115   fault zone. More recently, Maia et al. (2016) favored a southward propagation of the MAR into the transform

116   domain as a possible mechanism generating the large stepovers and associated thrust faults.

117
118   **3. Data**

119   In this work, we use 35 regional earthquakes with moment magnitude (M_W)>5.3 reported by the

120   GCMT since 2004 over Transforms A, B, and C. No earthquakes with M_W>5.3 were cataloged in Transform

121   D over the same time. The dataset includes permanent 3-component broad brand seismometers belonging to

122   the Brazilian Seismographic Network (RSBR, *Bianchi et al.* 2018), the IRIS/IDA (Incorporated Research

123   Institutions for Seismology) network (Scripps Institution of Oceanography, 1986), and GEOSCOPE

124   (doi:10.18715/GEOSCOPE.G). These networks were chosen based on the epicentral distance to the

125   earthquakes and the data availability (see map and histograms in Figure S04). In addition, we also included

126   data from temporary stations installed by the BLSP2002 project (*Feng et al.* 2004) in North-Northeast Brazil

127   to analyze earthquakes that happened in 2004-2005.

4. Methodology

4.1. Surface Waveform Modeling

We study the focal depth of the 35 earthquakes using a surface waveform model from records of 21 regional seismic stations at 1,000-3,050 km distance range (Figure 1b; Table S1; Figure S4). We only use stations where the Rayleigh waves present a good signal-to-noise ratio after filtering by a low-frequency filter (0.02-0.04 Hz). The waveform modeling was performed using an open-source MATLAB code package called ISOLA (*Sokos and Zahradnik* 2008; *Zahradnık and Sokos* 2018). The regional earthquakes used for modeling were chosen in the GCMT catalog based on two criteria: 1 – Data availability in networks; 2 – A magnitude threshold of M_W 5.3, which from our experience (*de Melo et al 2021; 2024*), provides signals with sufficiently high signal-to-noise ratio suitable for surface waveform model. All epicenter-station ray paths are represented in Figure S04, with the operation time of the stations.

A simple 1D crustal velocity model obtained from the CRUST1.0 global model (*Laske et al.* 2013) was used in ISOLA to model the surface waves in the oceanic crust (Table S2), with the model indicating a seafloor located 5.1 km below sea level. The model process starts with applying a 4th-degree Butterworth filter to remove the instrumental response and generate displacement waveforms in the frequency range of 0.02-0.04 Hz frequency range. In some cases, we modified the filter frequency range to 0.01-0.03 Hz for the farthest stations (e.g. DBIC and MPG; see Figure 1a). Next, a synthetic displacement waveform is generated for comparison, using the same filter frequency applied station by station. Green's functions were calculated using the AXITRA program (*Coutant* 1989), implemented in the ISOLA package. We used the fixed point-source ISOLA inversion, which fixes the strike/dip/range angles, applying focal mechanism angles provided by the GCMT catalog (*Dziewonski et al.* 1981; *Ekstrom et al.* 2012). ISOLA searches for the best solution across a source grid spaced at 1 km intervals.

Large strike-slip earthquakes should rupture along the PTDZ (*de Melo et al 2025*). Instead, we observed that the location of the GCMT epicenters are biased and occur sometimes several tens of kilometers away from the transform valley at Transform B and C (Figure S3). Pan and Dziewonski (2005) found that GCMT epicenters can be located up to half a degree from the proper tectonic plate borders. Therefore, we modified the epicentral coordinates, keeping the GCMT longitude, but moving the latitude onto the PTDZ mapped in multibeam data (*Maia et al 2016*). The distance between GCMT epicenter and the new modified epicenter vary from 0.44 to 20 km with average of 11.25 km (Figure 2). Recorded/synthetic waveform best-fitting solutions are described by the focal depth, centroid-time (CT), seismic moment (M_0), moment magnitude (M_W), CN (condition number which tells us whether the inversion problem is ill-posed, values <5 indicate the moment-tensor which is relatively well resolved), the double-couple percentage (DC) and 95% confidence interval VR (1). We estimate the depth uncertainties using a

161 computer code that expands the ISOLA package solutions (*Dias et al.* 2016), which applies several different

162 frequency ranges in the waveform inversion to reveal the stability and uncertainty of the solution of the

163 aforementioned centroid parameters considering a threshold (0.95) concerning the solution with the largest

164 VR. Three waveform-fitting examples of earthquakes with M_W 6.9, 5.9 and 5.7 are shown in Figures 3-5.

165 We used 4-10 stations during the analysis (Figure 6a; Table S3), depending on the data availability. The

166 mean 95% confidence interval for the earthquake waveform fitting shows VRs from 0.41 to 0.69, with most

167 vertical components often exceeding 0.90 (Figure 6b; Table S3). Most CN solutions of the earthquakes are

168 <4.5 (Figure 6c; Table S3), with the CTs obtained in analysis ranging from -0.2 to 4.8 s (Figure 6d; Table

169 S3). Changes in parameters like source-station orientation and velocity model provide new ISOLA solutions

170 with higher VR values. We used regional distance records, which makes it difficult to find an adequate

171 single velocity model to provide results with VRs close to 1.0 for all components (*de Melo et al 2021;*

172 *2024*). Nevertheless, low values of VR do not necessarily signify that a solution is ill-posed once ISOLA

173 considers fitted solutions with VR of 0.4 or more (*Zahradník and Sokos* 2018).

174

175 4.2. Thermal Structure Modeling

176 We employ the approach of the classical half-space cooling model to construct the thermal structure

177 of the SPTS. A geodynamic model can be found in Text S1 and Figure S5. The temperature field in the

178 cooling model is derived from the oceanic plate temperature formula (*Turcotte and Schubert 2014*):

179
$$T = T_s + (T_m - T_s)\left(1 - erfc\left(\frac{z}{2\sqrt{\kappa x/u}}\right)\right)$$

180 where T_s (0 °C) and T_m are temperatures of the surface and mantle, respectively, z is the depth from 0 at the

181 seafloor down to 200 km, κ is the thermal diffusivity (10^{-6} m^2/yr), x is the distance from the ridge axis, and

182 u is the spreading rate (27.8 mm/year; *DeMets et al 2010*). Previous studies reported that the mantle

183 temperature in the equatorial Atlantic might be ~150°C lower than elsewhere in the Atlantic Ocean (*Bonatti*

184 *1990; Bonatti et al. 1993; Schilling et al .1995; Hékinian et al. 2000; Le Voyer et al. 2015*). Consequently,

185 we tested two different potential mantle temperatures of 1150 and 1300°C. To account for thermal

186 transitions across transform offsets, the temperature field beneath each transform segment is modified by

187 averaging the temperatures of the adjacent ridge segments on both sides.

188 To evaluate the impact of different thermal structures, we extracted the depths of the 500°C, 600°C,

189 and 900°C isotherms from both models across three transform segments (A, B, and C). The comparison

190 between the two mantle temperature scenarios reveals significant spatial variations. Transform A exhibits

191 systematically shallower isotherms in areas away from the ridge in the 1300°C model (Figure 7a), indicating

192 a hotter lithosphere compared to the central region of the transform fault segment. In Transform B and C

193   (Figure 7b,c), the 500°C and 600°C isotherms show minimal differences, whereas the 900°C isotherm given

194   by the 1300°C model is notably shallower than Transform A due to the shorter offset area.

5. Results

The 35 events analyzed in Transforms A, B, and C show focal depths between 5±4 and 18±2 km bsf (Figure 8; Table S3). At Transform A, the magnitude of the 20 events ranges from 5.3 to 6.5 M_W. The focal depths vary between 5±3 km and 18±2 km bsf. Just two events were found in its western area of the Transform A, rupturing between 30.5° and 29.8° W longitudes, with the two epicenters of M_W 6.3 and 6.5 located close to each other, and focal depths at 9±3 and 10±5 km bsf, with an average of 9.5 km. Nine earthquakes are located beneath the Atobá Ridge between 29.6-28.6°W longitude, with focal depths ranging from 9±2 to 18±2 km bsf and an average of 14.3 km, most of them situated in the flanks of the Atobá Ridge, close to the mapped thrust faults. At the eastern end of Transform A between 28.5 to 27.75°W longitudes, eight strike-slip earthquakes presented focal depths with an average of 9.4 km, ranging from 6±4 to 14±2 km bsf, and their epicenters located in a deep basin crossed by the PTDZ. The zone is more linear and less segmented than the western and central areas of Transform A (*Maia et al.* 2016). Five events with moment magnitudes ranging from M_W 5.3-6.9 were analyzed for Transform B, providing an average of 7.8 km bsf. Two of the strike-slip earthquakes occur in the middle of the segment, with focal depths of 10±4 and 9±4 km bsf. The other two events are in the eastern domain close to the spreading segment separating the Transforms B and C, with focal depths of 6±3 km bsf for both earthquakes. Eight focal depth estimates are available for Transform C, with an average of 7.4 km bsf. The best-fitting waveforms show results with a 5-11 km depth range and a maximum uncertainty of 4 km, with most epicenters located over the restraining bends.

In general, our results from waveform modeling shows that the thickness of the seismogenic zone varies along the three transform segments (A, B, and C), with a maximum focal depth of 18 km. Wolfe et al. (1993) previously analyzed six earthquakes at Transform A, revealing focal depths of 8-14 km bsf. Our depth estimates are at least 3.5 km shallower than the depth reported in the GCMT catalog (Figure 7), which its common since GCMT does not consider the water layer in the depth analysis (*Ekström et al.* 2012). In our case, we assume the depth already removing the 5.1 km water layer of the CRUST1.0 (see *de Melo et al. 2021*). Just one earthquake that occurred in 2004-10-25 displayed focal depth deeper than those of the GCMT, which can be due to the poor seismographic network coverage during that period (Figure 1).

6. Discussion

6.1. Epicenter distribution along the Transforms A, B, and C

Oceanic transform faults may suffer from significant water percolation, thus inducing mantle rocks alteration (*Bonatti* 1976; *Francis et al.* 1978; *Detrick et al.* 1993; *Roland et al.* 2010). Serpentinization consistently reduces the bulk density and influences the strength and the tectonic style of the slow-spreading oceanic lithosphere (*Escartin et al.* 1997; *Escartin et al.* 2001). Bickert et al. (2023), for example, demonstrated that fluid-rock interactions take place under the Atoba Ridge, altering the rheology at Transform A. These effects govern the deformation and subsequently the activity in the Transform A region. Recent study have used teleseismic relative relocation to compare the earthquake distribution along globally oceanic transform faults, indicating that ~68% of the SPTS aseismically (*Shi et al 2021*). However, the author did not address transform segmentation along the St. Paul transform fault system, nor did he compare it to the local structure features offered by high resolution bathymetry.

We compared the new location of the earthquakes with the local structure presented by the multibeam data at Transform B and C. At Transform B, the five epicenters cover the PTDZ from its eastern RTI towards the center, indicating that a total of ~45% of the PTDZ is seismically active. Although we are using only five earthquakes, the same seismic coupling proportion apply compared to the entire GCMT catalog since 1990 (Figure S3). However, that proportion increase compared to nine earthquakes analyzed at Transform C, with the PTDZ seismically active for ~75% of the whole PTDZ extension. Additionally, the active area of the Transform C can increase to ~80% if we consider the whole GCMT catalog, suggesting that at least ~45% of the Transform B and ~75-80% of the Transform C extension are seismically active, contradicting the aseismic proportion provided by previous results (*Shi et al 2021*). Locals features such as a cold upper mantle could explain a different strength along the Transform A and B.

6.2. The focal depth distribution along the Transforms A, B, and C

The maximum depth of seismic faulting is controlled by the brittle to ductile transition which is itself a function of temperature. Early studies suggested that earthquakes along Atlantic transforms occur at shallow depth of ~4 km with no events occurring deeper than 7 km (*Engeln et al., 1986*). However, waveform inversion for focal mechanisms and focal depth, mostly based on teleseismic recordings, showed that these very shallow focal depths and little depth variation along a transform fault might not be correct. Instead, focal depth may vary profoundly along oceanic transform faults, with shallower earthquake

occurrence near ridge-transform intersections and deeper earthquakes in the center of segments. For example, Bergman and Solomon (1988) found that at the Charlie-Gibbs and Vema transform faults focal depths increase towards the center, deepening from 4-5 km near transform-ridge intersections (RTI) and reaching a maximum depths of 14-20 km bsf in the center of the transforms. Similar patterns are found by Fang and Abercrombie (2023) at the Chain transform in the equatorial Atlantic, revealing that earthquakes ruptured at~20-25 km near its center, while the shallower earthquakes clustered at 5-10 km near the RTIs. Abercrombie and Ekström (2001) also observed for the Chain transform focal depths of ~8-10 km near the RTI and ~12-16 km depth for earthquakes occurring away from both RTIs. At the Romanche transform, the longest transform fault in the equatorial Atlantic, they found identical pattern, though focal depth reached with 8-12 km and ~12-21 km somewhat deeper into the lithosphere at both RTIs and near its center, respectively.

The focal depths examined in our study are based on regional waveforms instead of teleseismic data and range from 5 to 18 km bsf along the Transforms A, B, and C of the St. Paul transform system. At Transform A, earthquakes in its central area and beneath the Atoba Ridge reach 9-18 km bsf, earthquakes closest to the western RTI reach 9-10 km bsf, and earthquakes near to the eastern RTI have a focal depth of 5-14 km bsf (Figure 8). We see focal depths of earthquakes ranging from 6 to 10 km along Transform B, with the deeper ones situated in the center (Figure 8). Earthquakes at Transform C display focal depths 5-11 km bsf (Figure 8). Therefore, our observations, in concert with previous investigations from teleseismic data (e.g., *Bergman and Solomon, 1988; Abercrombie and Ekström, 2001; Fang and Abercrombie, 2023*), provide a comprehensive understanding of how focal depths are distributed along transform faults revealing a systematic change of focal depths with deeper earthquakes occurring in the central area of transforms and shallow events near the RTIs.

6.3. Focal depth and thermal structure

Early seismic studies of oceanic transform faults found rather shallow focal depth, suggesting that earthquakes may occur at a similar thermal range (50-300°C) as those along continental faults (*Burr and Solomon, 1978*). The distribution of seismicity along both Chain and Romanche transform faults matches plate cooling thermal models, demonstrating the importance of temperature in determining focal depth and suggesting that most earthquakes occur with maximum depth related to the 600°C isotherm (*Abercrombie and Ekström 2001*). However, other studies suggested that some earthquakes may rupture at a higher temperature. For example, Bergman and Solomon (1988) suggested from their thermal models that

287   seismicity is limited to the thickness of the lithosphere (~900°C isotherm).

288   Morgan and Forsyth (1988) developed a 3-dimensional numerical model to explain seismicity
289   patterns in the mid-ocean ridge system with transform offsets, including the increase in earthquake
290   occurrence away from the RTIs towards the transform center. Their model, however, introduces an
291   isoviscous rheology, whereas modern geodynamic model studies favor nonlinear viscoplastic rheology,
292   which provides a better approximation of the mantle dynamics (*Behn et al., 2007; Liu et al., 2023*).
293   However, these models predict a strain localization that causes warm mantle upwelling beneath the
294   transform fault, which contradicts observations of deeper seismicity toward transform centers. One
295   potential explanation might be that active hydrothermal circulation along transform faults may dissipate
296   heat at their centers. Nevertheless, without independent evidence for the amount of hydrothermal mining
297   of heat, we instead use a 3-dimensional half-space cooling model to study the relationship between thermal
298   state and seismogenesis.

299   Our thermal model considers two thermal scenarios: a standard mantle temperature of 1300°C
300   commonly used in the literature and a colder mantle (1150°C) based on previous studies indicating a lower
301   mantle temperature in the equatorial Atlantic (*Bonatti 1990; Bonatti et al. 1993; Schilling et al .1995;*
302   *Hékinian et al. 2000; Le Voyer et al. 2015*). The model results show that the depth of the 600°C isotherm,
303   corresponding to the maximum depth of the brittle deformation (*Abercrombie and Ekström* 2001), increase
304   with transform offset length (Figure 9a,b). Transform A present the maximum depths, ~11 and 13 km bsf,
305   for 1300°C and 1150°C models, respectively (Figure 8). At Transform B, the 600°C isotherm is located at
306   depths of 7.9 and 9 km, and at Transform C, the isotherm reaches 6 and 7 km (Figure 8). For both thermal
307   scenarios, the deeper earthquakes are located above isotherms of 780-880°C at the center of the Transform
308   A, 660-750°C in Transform B, and 850-960°C in Transform C. Across all transforms, the depth of the
309   earthquakes increases with the modelled mantle temperature (Figure 9bc). Similarly, recent examinations
310   of focal depths using ocean-bottom seismometer data along the Chain transform fault revealed that the
311   seismogenic zone is deeper than the fault's maximum predicted depths in the center (*Leptokaropoulos et al.*
312   *2023; Schlaphorst et al. 2023*). These results suggest that the focal depth distribution compared with model
313   temperatures indicate that the seismic deformation occur inside a general range from ~600 to 900°C along
314   the length of the fault, reinforcing the idea that the center of transform faults is cooler than RTIs. In addition,
315   the half-space results assuming a colder mantle temperature (1150°C) fits better with observed focal depths
316   (Figure 8).

317   Our results suggest that the depth of seismogenic zone beneath Transforms A, B, and C agree with

expected maximum deformation presented by previous structural, geochemical, and seismological analyses (*Wolfe et al 1993; Roland et al. 2010; Barão et al 2020; Prigent et al. 2020; Bickert et al. 2023*). However, these results challenge the brittle weakening with viscoplastic mantle rheology done by Behn et al (2007), in which predicted warmer temperatures toward the middle of the transform caused by mantle upwelling and cooling toward the ridge segments (*Behn et al. 2007*). Instead, our observations support a cooler transform center, potentially influenced by hydrothermal activity and lower ambient mantle temperatures in the equatorial Atlantic.

Conclusion

We relocated earthquakes along the St. Paul transform fault system to the active fault using regional waveform modelling of surface waves and bathymetric data. From our analysis of focal depths and thermal modelling we conclude that

1.The strike-slip segments of the SPTS are strongly segmented revealing a considerable variation in seismic coupling, showing that between 45-80% of the mapped fault are seismically active.

2.The horizontal distribution of focal depths along Transforms A, B, and C reveals that the epicenters of the deepest earthquakes occur near the center zone of the PTDZs, whereas shallower focal depths are found near RTIs. These findings indicate that the horizontal distribution of seismic behavior at the St. Paul transform system is consistent with previous studies conducted on other transform faults such as Charlie-Gibbs, Vema, Romanche, and Chain.

3.Compared with the thermal model, the deepest earthquakes at the center zone of Transforms A, B, and C, are in colder area with lower temperatures along the PTDZ, contrary of the shallower earthquakes locating in hotter areas close to the RTI. These results support the existence of a colder upper mantle at center of the oceanic transform faults, challenging features issued by viscoplastic mantle rheology models.

Acknowledgments

GWSdM was funded by the European Union through MSCA-DN-ENVSEIS-101073148, and IG by ERC-TRANSFORMERS-101096190. GWSdM thanks for the rich comments and tips of Jiri Zahradnik about the surface waveform modeling, and Fabio Dias for supplying the code to calculate the depth uncertainties. We acknowledge the Resource Allocation Board, Germany for providing computational resources. Computations of thermal models in this study were performed on the supercomputers at NHR@ZIB under the projects SHK00051 and BBP00064. Thank Captain Gilles Ferrand and his crew and the COLMEIA scientific party for their help during the COLMEIA cruise. The COLMEIA ship time was financed by a grant from the Flotte océanographique française. Financial support for the cruise and preliminary data processing came from CNRS INSU Campagnes à la Mer and Labex Mer. Finally, thank you from our reviewers, David Schlaphorst and Pavla Hrubcová, who provided detailed comments that helped us to clarify some raised points in the text and figures, improving the manuscript.

Data Availability Statement

The broadband seismic waveform data of the Brazilian Seismographic Network (RSBR; Bianchi et al. 2018) network can be obtained at http://rsbr.on.br/request.html. The seismic data of the BLSP2002 project (*Feng et al 2004*), the GEOSCOPE network (*Romanowicz et al 1984*), and other global stations were downloaded from EarthScope Consortium Inc (*https://service.iris.edu/*). The ISOLA package (*http://seismo.geology.upatras.gr/isola/*) is applied for data processing and waveform models using MATLAB version 9.6 (*The MathWorks Inc. 2019*). The Global Centroid Moment Tensor database (*http://www.globalcmt.org*) was last accessed in March 2025. Maps and graphics were made with Generic Mapping Tools, version 6.6.0 (*Wessel et al.* 2019). Bathymetric data in Figure 1 was based on the Global Multi-Resolution Topography (GMRT; *Ryan et al. 2009*), version 4.3, available at https://www.gmrt.org/GMRTMapTool/, and accessed in February 2025. Additional Supplement Material information about the analysis for all earthquakes is accessible using the Zenodo repository (*de Melo et al. 2025*).

Author contribution

GWSM conducted the conceptualization, data curation, methodology and formal analysis of the waveform modeling, investigation, and validation of the focal depths. IG and MM contributed with supervision. SL developed the methodology, formal analysis, and validation of the thermal modeling. GWSdM, IG, SL, and MM contributed to the interpretation of the results. IG and LR provided funding acquisition and resources. GWSdM wrote the manuscript with contributions and reviews from all co-authors.

Competing interests.

380   The contact author has declared that none of the authors has any competing interests.

References

382   Abercrombie, R. E., & Ekström, G. (2001). Earthquake slip on oceanic transform faults. *Nature*, *410*(6824), 74-77.
383   https://doi.org/10.1038/35065064
384
385   Barão, L. M., Trzaskos, B., Angulo, R. J., & de Souza, M. C. (2020). Deformation and structural evolution of
386   mantle peridotites during exhumation on transform faults: A forced transition from ductile to brittle
387   regime. *Journal of Structural Geology*, *133*, 103981. https://doi.org/10.1016/j.jsg.2020.103981
388
389   Behn, M. D., Boettcher, M. S., & Hirth, G. (2007). Thermal structure of oceanic transform faults. *Geology*, *35*(4),
390   307-310. https://doi.org/10.1130/G23112A.1
391
392   Bergman, E. A., & Solomon, S. C. (1988). Transform fault earthquakes in the North Atlantic: Source mechanisms
393   and depth of faulting. *Journal of Geophysical Research: Solid Earth*, *93*(B8), 9027-9057.
394   https://doi.org/10.1029/JB093iB08p09027
395
396   Bianchi, M. B., Assumpção, M., Rocha, M. P., Carvalho, J. M., Azevedo, P. A., Fontes, S. L., ... & Costa, I. S.
397   (2018). The Brazilian seismographic network (RSBR): improving seismic monitoring in Brazil. *Seismological
398   Research Letters*, *89*(2A), 452-457. https://doi.org/10.1785/0220170227
399
400   Bickert, M., Kaczmarek, M. A., Brunelli, D., Maia, M., Campos, T. F., & Sichel, S. E. (2023). Fluid-assisted grain
401   size reduction leads to strain localization in oceanic transform faults. *Nature Communications*, *14*(1), 4087.
402   https://doi.org/10.1038/s41467-023-39556-5
403
404   Bonatti, E. (1976). Serpentinite protrusions in the oceanic crust. *Earth and Planetary Science Letters*, *32*(2), 107-
405   113. https://doi.org/10.1016/0012-821X(76)90048-0
406
407   Bonatti, E. (1990). Subcontinental mantle exposed in the Atlantic Ocean on St Peter–Paul
408   islets. *Nature*, *345*(6278), 800-802. https://doi.org/10.1038/345800a0
409
410   Bonatti, E., Seyler, M., & Sushevskaya, N. (1993). A cold suboceanic mantle belt at the Earth's
411   equator. *Science*, *261*(5119), 315-320. https://doi.org/10.1126/science.261.5119.315
412
413   Burr, N. C., & Solomon, S. C. (1978). The relationship of source parameters of oceanic transform earthquakes to
414   plate velocity and transform length. *Journal of Geophysical Research: Solid Earth*, *83*(B3), 1193-1205.
415   https://doi.org/10.1029/JB083iB03p01193
416
417   Campos, T. F., Bezerra, F. H., Srivastava, N. K., Vieira, M. M., & Vita-Finzi, C. (2010). Holocene tectonic uplift
418   of the St Peter and St Paul Rocks (Equatorial Atlantic) consistent with emplacement by extrusion. *Marine
419   Geology*, *271*(1-2), 177-186. https://doi.org/10.1016/j.margeo.2010.02.013
420
421   Campos, T. F., Sichel, S. E., Maia, M., Brunelli, D., Motoki, K., Magini, C., ... & de Melo, G. (2022). The singular
422   St. Peter and St. Paul Archipelago, equatorial Atlantic, Brazil. In *Meso-Cenozoic Brazilian Offshore
423   Magmatism* (pp. 121-165). Academic Press. https://doi.org/10.1016/B978-0-12-823988-9.00003-4
424
425   Coutant, O. (1989). Program of numerical simulation AXITRA. *Res. Rep. LGIT (in French), Universite Joseph
426   Fourier, Grenoble*.
427
428   DeMets, C., Gordon, R. G., & Argus, D. F. (2010). Geologically current plate motions. *Geophysical journal*

international, *181*(1), 1-80. https://doi.org/10.1111/j.1365-246X.2009.04491.x

de Melo, G. W. S., & Do Nascimento, A. F. (2018). Earthquake magnitude relationships for the Saint Peter and Saint Paul archipelago, equatorial atlantic. *Pure and Applied Geophysics*, *175*, 741-756. https://doi.org/10.1007/s00024-017-1732-6

de Melo, G. W. S., Mitchell, N. C., Zahradnik, J., Dias, F., & do Nascimento, A. F. (2021). Oceanic seismotectonics from regional earthquake recordings: the 4–5° N mid-Atlantic ridge. *Tectonophysics*, *819*, 229063. https://doi.org/10.1016/j.tecto.2021.229063

de Melo, G. W. S., Mitchell, N. C., & Sokolov, S. Y. (2024). The 2020 Mw 6.6 Vernadsky transform earthquake sequence: rupture and Coulomb stress changes surrounding an oceanic core complex. *Marine Geophysical Research*, *45*(4), 28. https://doi.org/10.1007/s11001-024-09558-z

de Melo, G. W. S., Grevemeyer, I., Lange, D., Metz, D., & Kopp, H. (2025). Relationship between rupture length and magnitude of oceanic transform fault earthquakes. *Geophysical Research Letters*, *52*(1), e2024GL112891. https://doi.org/10.1029/2024GL112891

de Melo, G. W. S., Grevemeyer, I., Liu, S., Maia, M., & Ruepke, L. (2025). Seismicity and thermal structure of the St. Paul Transform System, equatorial Atlantic: Insights from focal depth analysis [Dataset]. *Zenodo*. https://doi.org/10.5281/zenodo.15204422

Detrick, R. S., White, R. S., & Purdy, G. M. (1993). Crustal structure of North Atlantic fracture zones. *Reviews of Geophysics*, *31*(4), 439-458. https://doi.org/10.1029/93RG01952

Dias, F., Zahradník, J., & Assumpção, M. (2016). Path-specific, dispersion-based velocity models and moment tensors of moderate events recorded at few distant stations: examples from Brazil and Greece. *Journal of South American Earth Sciences*, *71*, 344-358. https://doi.org/10.1016/j.jsames.2016.07.004

Dziewonski, A. M., Chou, T. A., & Woodhouse, J. H. (1981). Determination of earthquake source parameters from waveform data for studies of global and regional seismicity. *Journal of Geophysical Research: Solid Earth*, *86*(B4), 2825-2852. https://doi.org/10.1029/JB086iB04p02825

Ekström, G., Nettles, M., & Dziewoński, A. M. (2012). The global CMT project 2004–2010: Centroid-moment tensors for 13,017 earthquakes. *Physics of the Earth and Planetary Interiors*, *200*, 1-9. https://doi.org/10.1016/j.pepi.2012.04.002

Engeln, J. F., Wiens, D. A., & Stein, S. (1986). Mechanisms and depths of Atlantic transform earthquakes. *Journal of Geophysical Research: Solid Earth*, *91*(B1), 548-577. https://doi.org/10.1029/JB091iB01p00548

Escartin, J., Hirth, G., & Evans, B. (1997). Effects of serpentinization on the lithospheric strength and the style of normal faulting at slow-spreading ridges. *Earth and Planetary Science Letters*, *151*(3-4), 181-189. https://doi.org/10.1016/S0012-821X(97)81847-X

Escartin, J., Hirth, G., & Evans, B. (2001). Strength of slightly serpentinized peridotites: Implications for the tectonics of oceanic lithosphere. *Geology*, *29*(11), 1023-1026. https://doi.org/10.1130/0091-7613(2001)029%3C1023:SOSSPI%3E2.0.CO;2

Fang, H., & Abercrombie, R. E. (2023). SMatStack to enhance noisy teleseismic seismic phases: Validation and application to resolving depths of oceanic transform earthquakes. *Geochemistry, Geophysics, Geosystems*, *24*(11), e2023GC011109. https://doi.org/10.1029/2023GC011109

Feng, M., Assumpçao, M., & Van der Lee, S. (2004). Group-velocity tomography and lithospheric S-velocity structure of the South American continent. *Physics of the Earth and Planetary Interiors*, *147*(4), 315-331. https://doi.org/10.1016/j.pepi.2004.07.008

Francis, T. J. G., Porter, I. T., & Lilwall, R. C. (1978). Microearthquakes near the eastern end of St Paul's Fracture Zone. *Geophysical Journal International*, *53*(2), 201-217. https://doi.org/10.1111/j.1365-246X.1978.tb03738.x

Hekinian, R., Juteau, T., Gracia, E., Sichler, B., Sichel, S., Udintsev, G., ... & Ligi, M. (2000). Submersible observations of equatorial atlantic mantle: the St. Paul Fracture Zone region. *Marine Geophysical Researches*, *21*, 529-560. https://doi.org/10.1023/A:1004819701870

Laske, G., Masters, G., Ma, Z., & Pasyanos, M. (2013, April). Update on CRUST1. 0—A 1-degree global model of Earth's crust. In *Geophysical research abstracts* (Vol. 15, No. 15, p. 2658).

Le Voyer, M., Cottrell, E., Kelley, K. A., Brounce, M., & Hauri, E. H. (2015). The effect of primary versus secondary processes on the volatile content of MORB glasses: An example from the equatorial Mid-Atlantic Ridge (5 N–3 S). *Journal of Geophysical Research: Solid Earth*, *120*(1), 125-144. https://doi.org/10.1002/2014JB011160

Leptokaropoulos, K., Rychert, C. A., Harmon, N., Schlaphorst, D., Grevemeyer, I., Kendall, J. M., & Singh, S. C. (2023). Broad fault zones enable deep fluid transport and limit earthquake magnitudes. *Nature Communications*, *14*(1), 5748. https://doi.org/10.1038/s41467-023-41403-6

Liu, S., Guo, Z., Rüpke, L. H., Morgan, J. P., Grevemeyer, I., Ren, Y., & Li, C. (2023). Sensitivity of gravity anomalies to mantle rheology at mid-ocean ridge–transform fault systems. *Earth and Planetary Science Letters*, *622*, 118420. https://doi.org/10.1016/j.epsl.2023.118420

Maia, M., Sichel, S., Briais, A., Brunelli, D., Ligi, M., Ferreira, N., ... & Oliveira, P. (2016). Extreme mantle uplift and exhumation along a transpressive transform fault. *Nature Geoscience*, *9*(8), 619-623. https://doi.org/10.1038/ngeo2759

Melson, W. G., Jarosewich, E., Bowen, V. T., & Thompson, G. (1967). St. Peter and St. Paul Rocks: a high-temperature, mantle-derived intrusion. *Science*, *155*(3769), 1532-1535. https://doi.org/10.1126/science.155.3769.1532

Morgan, J. P., & Forsyth, D. W. (1988). Three-dimensional flow and temperature perturbations due to a transform offset: Effects on oceanic crustal and upper mantle structure. *Journal of Geophysical Research: Solid Earth*, *93*(B4), 2955-2966. https://doi.org/10.1029/JB093iB04p02955

Pan, J., Antolik, M., & Dziewonski, A. M. (2002). Locations of mid-oceanic earthquakes constrained by seafloor bathymetry. *Journal of Geophysical Research: Solid Earth*, *107*(B11), EPM-8. https://doi.org/10.1029/2001JB001588

Pan, J., & Dziewonski, A. M. (2005). Comparison of mid-oceanic earthquake epicentral differences of travel time, centroid locations, and those determined by autonomous underwater hydrophone arrays. *Journal of Geophysical Research: Solid Earth*, *110*(B7). https://doi.org/10.1029/2003JB002785

Prigent, C., Warren, J. M., Kohli, A. H., & Teyssier, C. (2020). Fracture-mediated deep seawater flow and mantle hydration on oceanic transform faults. *Earth and Planetary Science Letters*, *532*, 115988. https://doi.org/10.1016/j.epsl.2019.115988

Ren, Y., Lange, D., & Grevemeyer, I. (2023). Seismotectonics of the Blanco transform fault system, northeast Pacific: Evidence for an immature plate boundary. *Journal of Geophysical Research: Solid Earth*, *128*(3), e2022JB026045. https://doi.org/10.1029/2022JB026045

Roland, E., Behn, M. D., & Hirth, G. (2010). Thermal-mechanical behavior of oceanic transform faults: Implications for the spatial distribution of seismicity. *Geochemistry, Geophysics, Geosystems*, *11*(7). https://doi.org/10.1029/2010GC003034

Romanowicz, B., Cara, M., Fel, J. F., & Rouland, D. (1984). GEOSCOPE: A French initiative in long-period three-component global seismic networks. *Eos, Transactions American Geophysical Union*, *65*(42), 753-753. https://doi.org/10.1029/EO065i042p00753-01

Ryan, W. B., Carbotte, S. M., Coplan, J. O., O'Hara, S., Melkonian, A., Arko, R., ... & Zemsky, R. (2009). Global multi-resolution topography synthesis. *Geochemistry, Geophysics, Geosystems*, *10*(3). https://doi.org/10.1029/2008GC002332

Sautter, B., Escartin, J., Petersen, S., Gaina, C., Granot, R., & Pubellier, M. (2024). *MAPRIDGES: global database of Mid-Oceanic ridges segments and transform faults. SEANOE.* https://doi.org/10.17882/99981

Schilling, J. G., Ruppel, C., Davis, A. N., McCully, B., Tighe, S. A., Kingsley, R. H., & Lin, J. (1995). Thermal structure of the mantle beneath the equatorial Mid-Atlantic Ridge: Inferences from the spatial variation of dredged basalt glass compositions. *Journal of Geophysical Research: Solid Earth*, *100*(B6), 10057-10076. https://doi.org/10.1029/95JB00668

Schlaphorst, D., Rychert, C. A., Harmon, N., Hicks, S. P., Bogiatzis, P., Kendall, J. M., & Abercrombie, R. E. (2023). Local seismicity around the Chain Transform Fault at the Mid-Atlantic Ridge from OBS observations. *Geophysical Journal International*, *234*(2), 1111-1124. https://doi.org/10.1093/gji/ggad124

Shi, P., Wei, M., & Pockalny, R. A. (2022). The ubiquitous creeping segments on oceanic transform faults. *Geology*, *50*(2), 199-204. https://doi.org/10.1130/G49562.1

Sokos, E. N., & Zahradnik, J. (2008). ISOLA a Fortran code and a Matlab GUI to perform multiple-point source inversion of seismic data. *Computers & Geosciences*, *34*(8), 967-977. https://doi.org/10.1016/j.cageo.2007.07.005

Turcotte, D., & Schubert, G. (2014). *Geodynamics* (3rd ed.). Cambridge: Cambridge University Press. https://doi.org/10.1017/CBO9780511843877

The MathWorks Inc. (2019). MATLAB version: 9.6 (R2019a) [Software]. The MathWorks Inc. https://www.mathworks.com

Vincent, C., Maia, M., Briais, A., Brunelli, D., Ligi, M., & Sichel, S. (2023). Evolution of a Cold Intra-Transform Ridge Segment Through Oceanic Core Complex Splitting and Mantle Exhumation, St. Paul Transform System, Equatorial Atlantic. *Geochemistry, Geophysics, Geosystems*, *24*(5), e2023GC010870. https://doi.org/10.1029/2023GC010870

Wessel, P., Luis, J. F., Uieda, L. A., Scharroo, R., Wobbe, F., Smith, W. H., & Tian, D. (2019). The generic mapping tools version 6. *Geochemistry, Geophysics, Geosystems*, *20*(11), 5556-5564. https://doi.org/10.1029/2019GC008515

Wolfe, C. J., Bergman, E. A., & Solomon, S. C. (1993). Oceanic transform earthquakes with unusual mechanisms or locations: relation to fault geometry and state of stress in the adjacent lithosphere. *Journal of Geophysical*

Research: Solid Earth, *98*(B9), 16187-16211. https://doi.org/10.1029/93JB00887

Zahradník, J., & Sokos, E. (2018). ISOLA code for multiple-point source modeling. *Moment tensor solutions: A useful tool for seismotectonics*, 1-28. https://doi.org/10.1007/978-3-319-77359-9_1

Figure 1: a) Geographical location of the area in study along the equatorial Atlantic Ocean. b) Regional bathymetric map of the equatorial Atlantic. Oceanic transform faults are presented by red lines, while the mid-ocean ridges are shown in black lines (Sautter et al. 2024). The white box refers to the Saint Paul Transform System (SPTS, *Maia et al.* 2016), shown in c). White circles represent the epicentral catalog of the International Seismological Centre between 1990 and 2022 (Weston et al, 2018). Black triangles indicates the seismic stations used in this study (more detail in Data chapter and Figure S04). Earthquakes with M_W >5.3 occurred since 1990 cataloged by the GCMT and analyzed in this study are shown in red stars. b) Bathymetric map of the St. Paul Transform System. The GCMT events with M_W >5.3 used in this study are presented by the red beachballs, while the black beach balls refer to the whole GCMT M_W >5.3 since 1990. Gray beach balls refer to the events analyzed by Wolfe et al (1993). White lines refer to the transform fault segments along the SPTS, while the red lines refer to the intra-transform ridge axis (Maia et al. 2016). The continuous white dashed lines refer to the fracture zones.

Figure 2: Bathymetric map of the moved epicenters. White lines show the transform faults, while the intra-transform ridges are shown in red lines (Maia et al. 2016). Squares are the initial GCMT epicenter, with the moved location used on the waveform model presented by the circle symbols. The arrows connect the GCMT locations to the final locations, with a mislocation average of 11.25 km away.
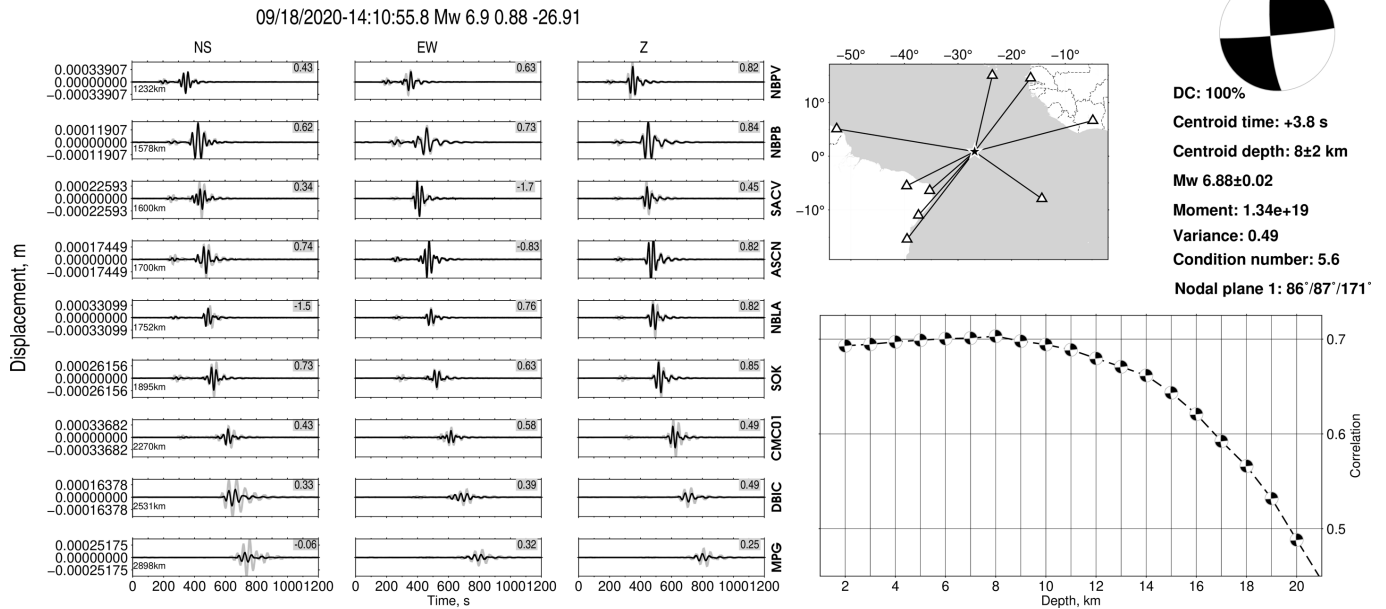
648
649
650 Figure 3: Focal depth analysis in SPTS of the Mw 6.9 earthquake occurred at Transform B in 09/18/2020. Left figure:
651 Waveforms (gray) and their models (black) obtained with the best-fitting source position at 8 km depth. Middle upper
652 figure: epicentral location map with their specified source-data ray paths for the respective seismic stations used on
653 ISOLA analysis. Downright figure: Correlation vs Depth for the earthquake. The best solutions referent to each of the
654 two earthquakes were fitted with higher correlation at 8±2 km depth.

655
656
657
658
659
660
661
662
663
664
665
666
667
668
669
670
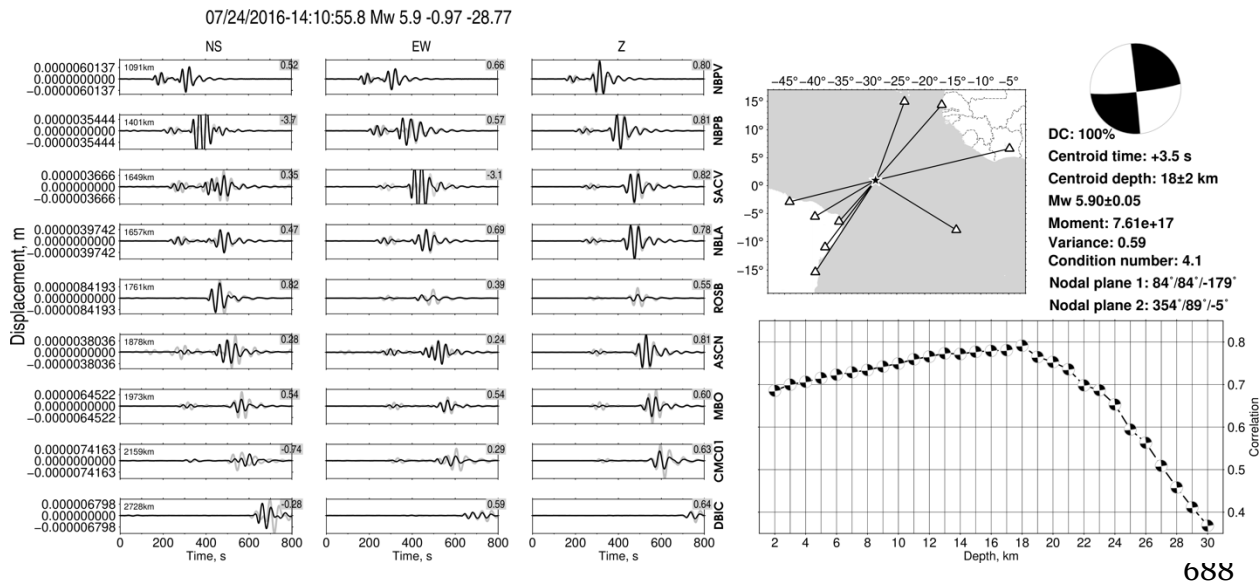
Figure 4: Focal depth analysis in SPTS of the Mw 5.9 earthquake occurred at Transform A in 07/24/2016. Left figure: Waveforms (gray) and their models (black) obtained with the best-fitting source position at 18 km depth. Middle upper figure: epicentral location map with their specified source-data ray paths for the respective seismic stations used on ISOLA analysis. Downright figure: Correlation vs Depth for the earthquake. The best solutions referent to each of the two earthquakes were fitted with higher correlation at 18±2 km depth.
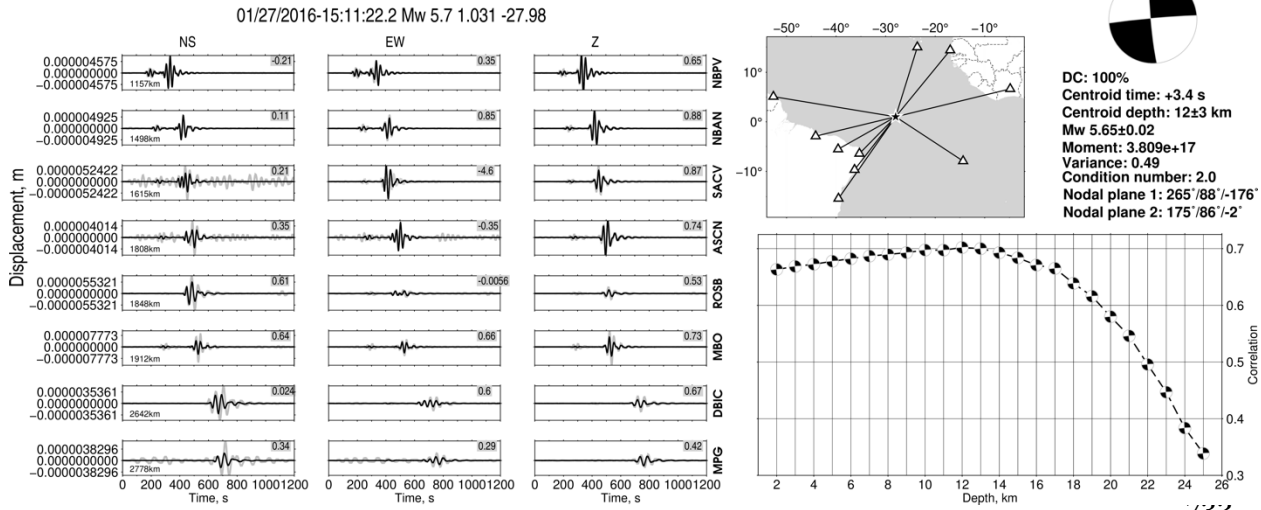
733
734 Figure 5: Focal depth analysis in SPTS of the Mw 5.7 earthquake occurred at Transform A in 01/27/2016. Left figure:
735 Waveforms (gray) and their models (black) obtained with the best-fitting source position at 12 km depth. Middle
736 upper figure: epicentral location map with their specified source-data ray paths for the respective seismic stations
737 used on ISOLA analysis. Downright figure: Correlation vs Depth for the earthquake. The best solutions referent to
738 each of the two earthquakes were fitted with higher correlation at 12±3 km depth.
739
740
741
742
743
744
745
746
747
748
749
750
751
752
753
754
755
756
757
758
759
760
761
762
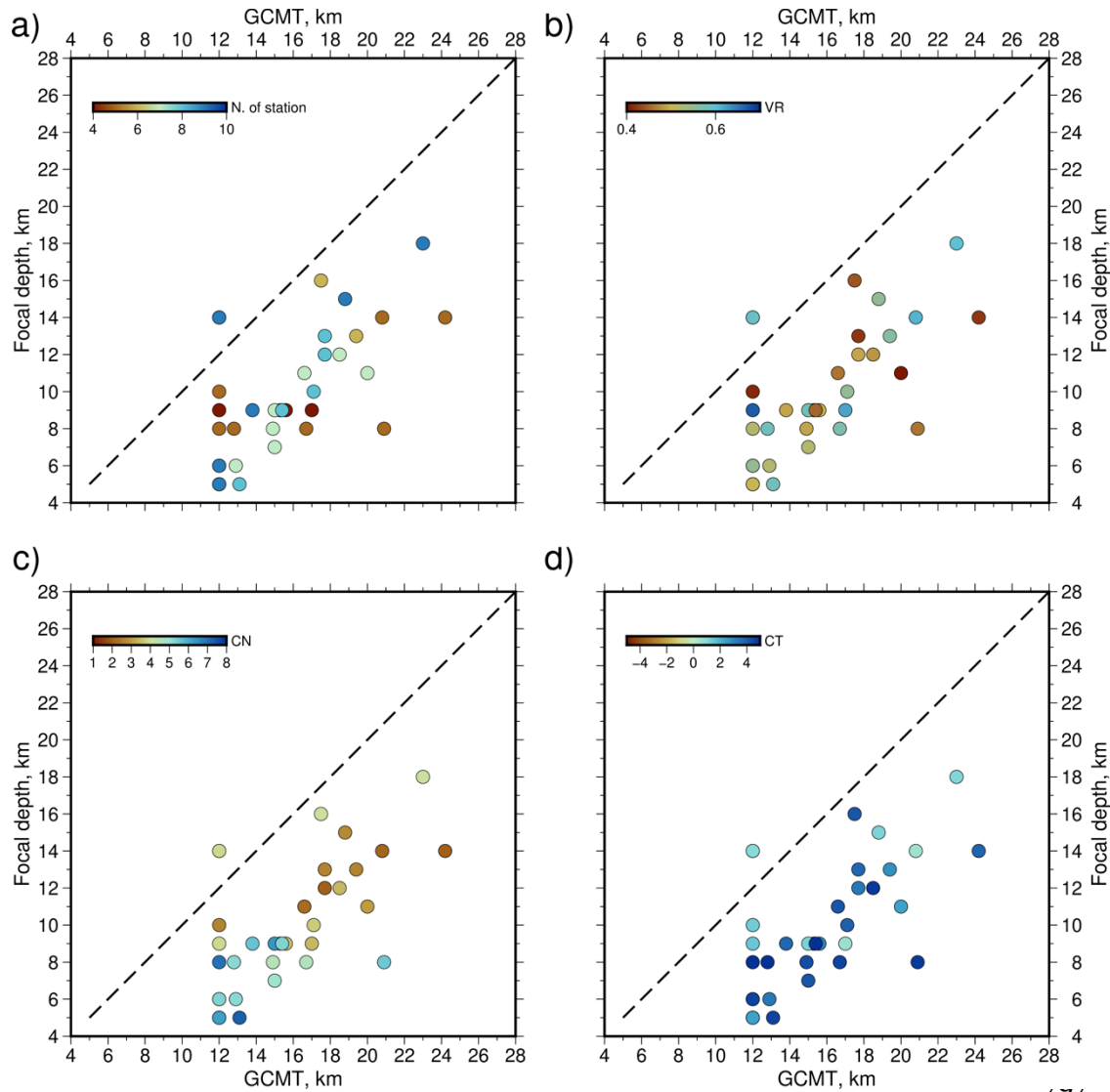
Figure 6: Comparison of the focal depth analyzed in SPTS using regional records versus GCMT depth. a) Comparison with the number of stations used in the analysis, presented by the symbol colors. Most of the earthquake had a minimum of six stations used in analysis, with most of the solutions presenting a synthetic/real waveform fitting with VR>0.5 (b). c) Symbol color showing the variation of the condition number (CN) of the ISOLA solution referent to each earthquake. Most solutions had CN<5. d) Comparison with the centroid-time (CT) obtained in waveform fitting, with most events presenting CT>0, indicating the existence of a difference between the origin time of the moment tensor solutions of the GCMT with the CT obtained using the regional stations.
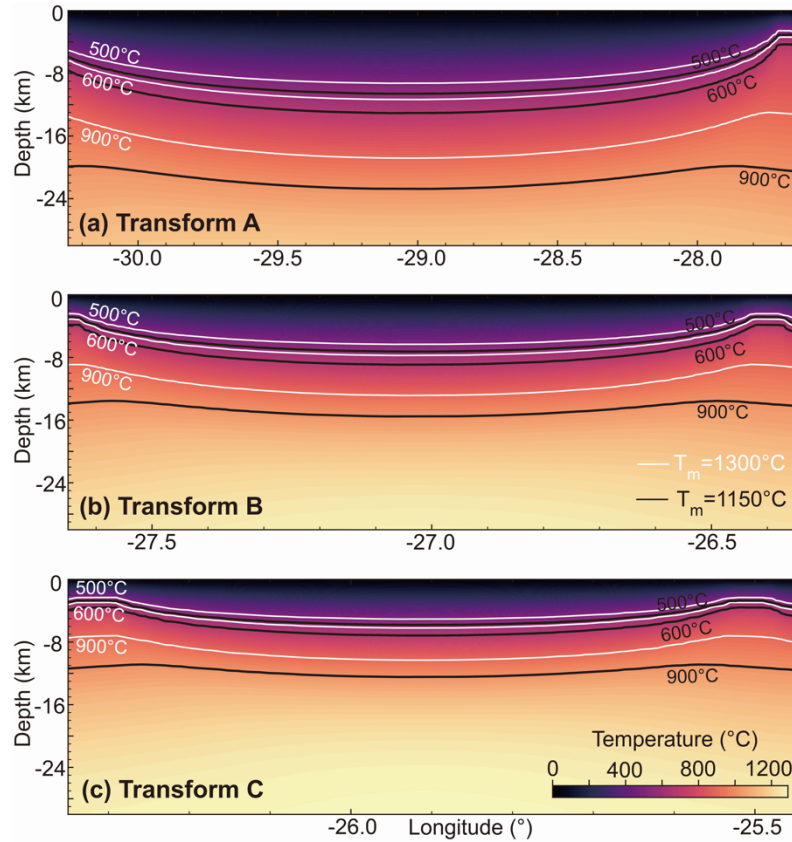
Figure 7: Half-space cooling model (HSCM) referent to Transforms A, B, and C (a/b/c). Black lines refer to the model calculated assuming a mantle temperature of 1150°C, referent to the respective maximum serpentinization depth at transform segments (500°C, Maia et al 2016); the 600°C referent to the expected maximum brittle-ductile transition (Abercrombie and Ekström 2001); and the limitation of the deep fluid-rock interaction with influence in deformation expected to occur until 900°C (Prigent et al. 2020; Bickert et al. 2023). White lines indicate the results obtained for the same isotherms, but assuming the 1300°C mantle temperature on HSCM. Due to the long-offset difference between the three transform segments, we can observe a considerable variation between the depth of the isotherms.
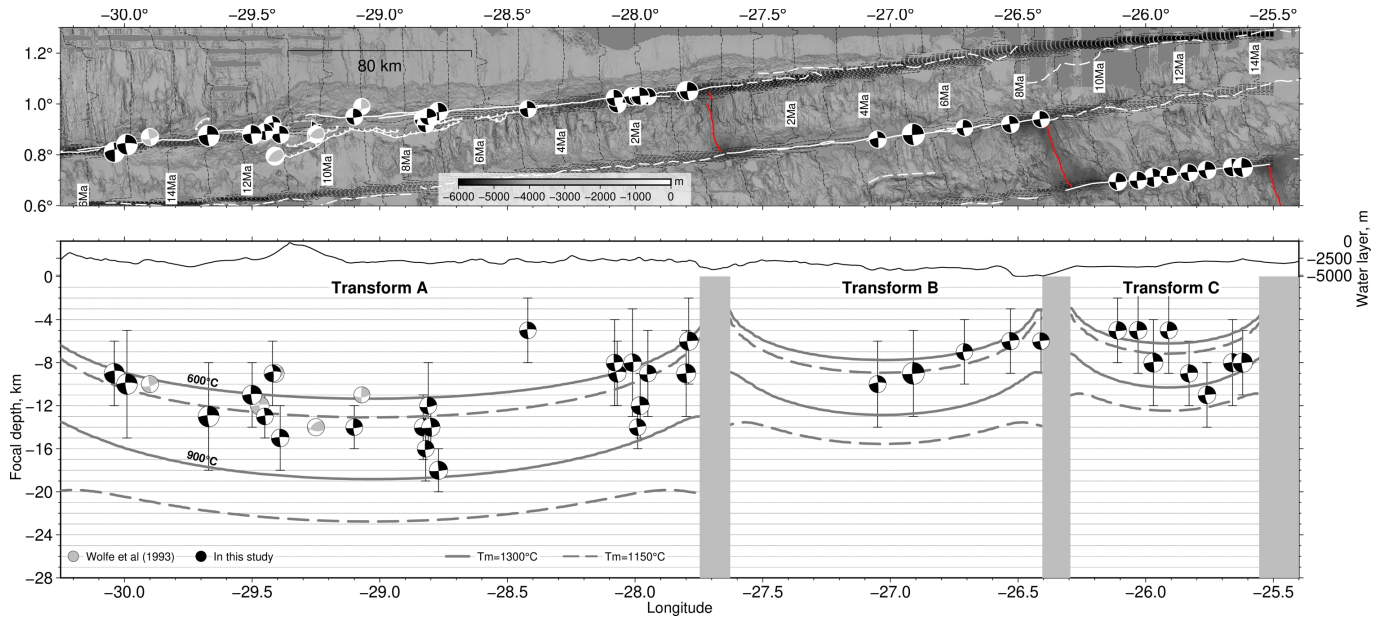
Figure 8: Earthquake focal depth distribution along the St. Paul transform system. Upper panel: Bathymetric map of the transform segments A, B, C. White lines refer to the transform faults, while red lines show the mid-ocean ridges tectonic plate boundaries mapped by Maia et al (2016). White dashed lines indicate the fracture zones. Black dashed lines show the crustal age variation in the St. Paul transform system (see Figure S01), calculated by Maia et al (2016). The epicenter locations of the 32 events of the GCMT catalog with M_W >5.3 are presented by the black beachballs. Gray beach balls refer to the earthquakes reported by Wolfe et al (1993) with a magnitude of 5.1<mb<5.9 (5.2< M_W <6.0; Kim et al. 2024). Bottom panel: cross-section of the Transform A, B, and C segments following the map longitude range, with the vertical distribution of the 32 earthquakes analyzed in this study (black beachballs) and the five earthquakes reported by Wolfe et al (1993). Vertical uncertainties of the focal depths varying from 2 to 5 km are presented by the thinner vertical black lines. The gray isotherms lines indicate the thermal structure for temperatures of 600, and 900°C beneath the SPTS assuming the mantle temperature of 1300°C, while the dashed gray lines refer to the mantle temperature of 1150°C. In both two models, at least 18 earthquakes are located at depths deeper than the 600°C isotherm, the predicted brittle-ductile transition beneath the oceanic transform faults (Abercrombie and Ekstrom. 2001).
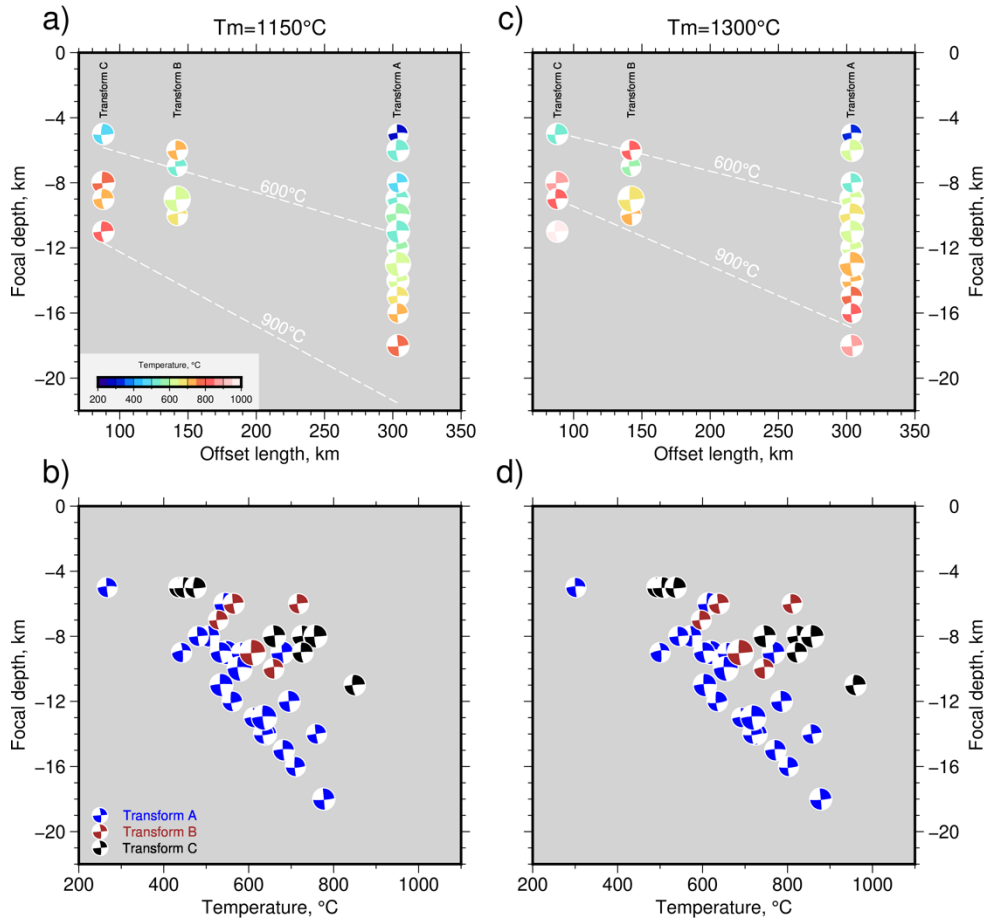
Figure 9: a/b Comparison of the focal depth with the offset length of the Transform A, B, C (Ren et al 2021) and calculated temperatures, respectively. A mantle temperature of 1150°C was assumed for results presented in both a) and b). Results obtained using a hotter mantle temperature of 1300°C is shown in c) and d). We can observe a gradual increase of the maximum focal depth with the increase of the offset length, which is expected to occur along the half-space cooling.